J. Fluid Mech. (2007), *vol.* 590, *pp.* 187–208.
doi:10.1017/S0022112007008038 Printed in the United Kingdom

Onset of convection in a moderate aspect-ratio rotating cylinder: Eckhaus–Benjamin–Feir instability

J. M. LOPEZ,[1] F. MARQUES,[2] I. MERCADER[2] AND O. BATISTE[2]

[1]Department of Mathematics and Statistics, Arizona State University, Tempe, AZ 85287, USA
[2]Departament de Física Aplicada, Univ. Politècnica de Catalunya, Barcelona 08034, Spain

(Received 12 July 2006 and in revised form 19 June 2007)

A numerical study of the onset of thermal convection in a rotating circular cylinder of radius-to-depth ratio equal to four is considered in a regime dominated by the Coriolis force where the onset is to so-called wall modes. The wall modes consist of hot and cold pairs of thermal plumes rising and descending in the cylinder wall boundary layer, forming an essentially one-dimensional pattern characterized by the number of hot/cold plume pairs, m. In the limit of zero centrifugal force, this onset of convection at a critical temperature difference across the depth of the cylinder is via a symmetry-breaking supercritical Hopf bifurcation which leads to retrograde precession of the pattern with respect to the rotation of the cylinder. For temperature differences greater than critical, a number of distinct wall modes, distinguished by m, coexist and are stable. Their dynamics are controlled by an Eckhaus–Benjamin–Feir instability, the most basic features of which had been captured by a complex Ginzburg–Landau equation model. Here, we analyse this instability in rotating convection using direct numerical simulations of the Navier–Stokes equations in the Boussinesq approximation. Several properties of the wall modes are computed, extending the results to far beyond the onset of convection. Extensive favourable comparisons between our numerical results and previous experimental observations and complex Ginzburg–Landau model results are made.

1. Introduction

Rotating Rayleigh–Bénard convection (RRBC) encompasses the competition between rotation and thermal buoyancy which is central to a range of hydrodynamic situations including astrophysical and geophysical flows, as well as being readily accessible at laboratory scales for detailed experimental investigations. The development of the current understanding of RRBC has taken a peculiar path, in part due to the large variety of possible nonlinear behaviour near the onset of convection, and also due to the theoretical and numerical tools available at the time, making idealizations in the modelling of the flow necessary and consequently influencing the design of experiments (Hu, Ecke & Ahlers 1997).

The main idealization in convection problems is the Boussinesq approximation which only accounts for density variations in the buoyancy terms of the governing equations. This allows for the use of analytic and numerical techniques for incompressible hydrodynamics. Its appropriateness has been extensively tested and

verified, particularly when the temperature difference across the layer is small (e.g. see the review by Bodenschatz, Pesch & Ahlers 2000, and references therein). Another main idealization used in the early studies was to consider the convection of fluid in a laterally unbounded but periodic layer. While this makes the linear stability analysis of the conduction state straightforward (see Chandrasekhar 1961, for an extensive summary of these studies), it introduces shortcomings, particularly for the rotating convection problem. The idealized horizontal periodicity precludes the consideration of the effects of the centrifugal force, whose strength varies with the radial distance from the axis of rotation, and so only the effects of the Coriolis force can be studied. Furthermore, the effects of lateral confinement are also not accounted for. The experiments of Rossby (1967) found significant discrepancies with the unbounded theory for the onset of convection, measuring convective heat transfer at Rayleigh numbers much lower than predicted. Buell & Catton (1983) and Pfotenhauer, Niemela & Donnelly (1987), based on linear stability analysis and experiments, proposed that the cause of the discrepancy was due to the presence of lateral confinement. Subsequent experiments, designed to allow for flow visualization (Zhong, Ecke & Steinberg 1991, 1993; Ning & Ecke 1993), showed that the convective heat transport recorded at Rayleigh numbers below the predicted critical value was due to a so-called convective wall mode, consisting of alternating hot and cold thermal plumes rising and descending in the cylinder sidewall boundary layer, and precessing retrograde with respect to the rotation of the cylinder. The linear stability analysis of Goldstein *et al.* (1993, 1994) confirmed this picture of the onset of RRBC due to the combined effects of Coriolis force and lateral confinement in a finite cylinder. The nonlinear behaviour of RRBC just beyond onset, however, presents a challenging problem owing to the co-existence of multiple stable nonlinear states.

Herrmann & Busse (1993) and Kuo & Cross (1993) considered a model problem which analysed the flow local to a lateral wall neglecting curvature, which amounted to having the axis of rotation infinitely far away from the wall. They were able to show that the observed onset of RRBC below the predicted critical Rayleigh number could be accounted for by the Coriolis force and the presence of a lateral wall, even if the wall was far from the rotation axis.

The nonlinear dynamics of the wall modes are significantly influenced by the symmetry of the problem, e.g. their onset breaks the invariance under rotations about the rotation axis and this symmetry breaking is the root cause of the observed precession of the flow pattern (Ecke, Zhong & Knobloch 1992). It was recognized early on that the weakly nonlinear behaviour of the wall modes fit the framework of the Eckhaus instability (Eckhaus 1965), and that due to the precession of the pattern at onset, had analogies with the Benjamin–Feir instability (Benjamin & Feir 1967) and could be modelled via the complex Ginzburg–Landau equation (Ning & Ecke 1993; Liu & Ecke 1997, 1999). The discreteness of the wavenumber due to the periodicity of the azimuthal direction suggests that analogous effects due to discrete spectra in the real Ginzburg–Landau equation described in Ahlers *et al.* (1986) and Tuckerman & Barkley (1990) can be expected to play a role in RRBC.

Janiaud *et al.* (1992) also investigated the Eckhaus–Benjamin–Feir (EBF) instability of travelling waves. The basic state in their system consisted of concentric convection rolls in an annulus which were forced to be axisymmetric under some conditions by a thin resistive wire placed on the outer cylinder wall which provided a controlled radial temperature gradient when a voltage was applied. This basic state has $O(2)$ symmetry in azimuth, i.e. it is invariant to arbitrary rotations about the axis and to reflections in a meridional plane. When the system bifurcates to three-dimensional,

waves appear on the rolls with a discrete azimuthal wavenumber. Above criticality, there are a number of three-dimensional states with a band of wavenumbers that are stable. These waves may rotate in either the clockwise or counterclockwise direction since it is the $O(2)$ symmetry that is being broken (Knobloch 1994), and standing waves are also possible but apparently not observed in these experiments. At about the same time, the wall modes in RRBC were identified, and this problem only has $SO(2)$ symmetry in azimuth, owing to the bias provided by the rotation, and hence the wall modes rotate in one direction only. Hence, the study of the EBF instability of the wall modes is somewhat more straightforward than in the problem studied by Janiaud *et al.* (1992).

Flow visualization is difficult to achieve in RRBC experiments very near onset. Furthermore, since the wall modes are due to the Coriolis force in the presence of a lateral boundary and the centrifugal force tends to quench the wall mode (we have preliminary numerical results showing this quenching, which we shall report in detail elsewhere), experiments have been restricted to quite small Coriolis force and/or small aspect ratio cylinders in order to keep the centrifugal force negligible. A consequence of the restriction to small Coriolis force is that the range of temperature differences across the layer over which wall modes are present without any convective motion in the bulk diminishes with decreasing Coriolis force; see figure 2 of Liu & Ecke (1999). In order to explore the EBF instability over a large range of azimuthal wavenumbers it is then desirable to have a large Coriolis force or a cylinder of large radius-to-depth aspect ratio, but both of these lead to large centrifugal effects. Numerically, there is no problem in setting the centrifugal force to zero while incorporating a sizeable Coriolis force. In fact, the vast majority of numerical studies of RRBC do this.

It is only relatively recently that theoretical and numerical studies of the wall mode have been conducted implementing realistic no-slip boundary conditions. These studies include Plaut (2003), whose theoretical model neglected curvature effects, and Choi *et al.* (2004) whose numerical model also neglected curvature effects. Both studies focused on determining the marginal stability curve for the onset of wall modes together with some weakly nonlinear analysis with the aim of estimating the coefficients in a complex Ginzburg–Landau equation model of the problem. The resulting envelope equation models were successful in reproducing some aspects very near onset, but a number of discrepancies with experimental observations were partially attributed to the neglect of curvature effects. Neither study investigated the EBF instability. At about the same time, Scheel *et al.* (2003) conducted a numerical investigation using realistic no-slip boundary conditions in an annular geometry, also with the aim of estimating the coefficients in a complex Ginzburg–Landau model of the problem. Sánchez-Álvarez *et al.* (2005) computed RRBC in a cylindrical geometry using realistic boundary conditions, and have reported some examples of wall modes, as well as bulk modes displaying Kuppers–Lörtz type domain chaos and other more regular bulk patterns, in good agreement with the experimental observations reported in Bajaj *et al.* (1998). However, neither of the numerical studies which included curvature effects addressed the EBF instability of the wall modes.

In this paper, we present a nonlinear numerical study, using the Navier–Stokes–Boussinesq equations with realistic no-slip boundary conditions in a cylindrical geometry, of the effects of large Coriolis force on the onset of RRBC via wall modes, and their EBF instability. The results are in very good agreement with the comprehensive experimental observations reported in Liu & Ecke (1997, 1999), for similar but slightly larger values of the aspect ratio and smaller rotation rates. Our

results with stronger Coriolis force lend further support to their description of the nonlinear dynamics associated with the Coriolis force near the onset of RRBC.

2. Governing equations and numerical scheme

We consider the flow in a circular cylinder of radius r_0 and depth d, rotating at a constant rate ω rad s^{-1}. The top endwall is maintained at a constant temperature $T^* = T_0 - 0.5\Delta T$ and the bottom endwall at a constant temperature $T^* = T_0 + 0.5\Delta T$. The Boussinesq approximation is implemented, which treats all fluid properties as constant, except for the density in the buoyancy terms which are comprised of the gravitational and the centrifugal buoyancies. To lowest order, the density varies linearly with temperature, i.e.

$$\rho = \rho_0(1 - \alpha(T^* - T_0)), \tag{2.1}$$

where T_0 is the mean temperature and ρ_0 is the density at that temperature. In the rotating frame of reference, the governing equations are

$$(\partial_t + \boldsymbol{u}\cdot\nabla)\boldsymbol{u} = -\nabla P/\rho_0 + \nu\nabla^2\boldsymbol{u} + g\alpha T\hat{z} + 2\omega\boldsymbol{u}\times\hat{z} - \omega^2\alpha T\boldsymbol{r}, \tag{2.2}$$

$$(\partial_t + \boldsymbol{u}\cdot\nabla)T = \kappa\nabla^2 T, \tag{2.3}$$

$$\nabla\cdot\boldsymbol{u} = 0, \tag{2.4}$$

where $\boldsymbol{u}$ is the velocity field, $T = T^* - T_0$ is the temperature deviation with respect to the mean temperature, P is the dynamic pressure which incorporates the hydrostatic pressure due to the gravitational and centrifugal forces, g is the acceleration due to gravity, α is the coefficient of volume expansion, ν is the kinematic viscosity, $\boldsymbol{r}$ is the radial vector in cylindrical coordinates, and $\hat{z}$ the unit vector in the vertical direction z.

The system is non-dimensionalized using d as the length scale, d^2/κ as the time scale, where κ is the thermal diffusivity, and ΔT as the temperature scale. There are five non-dimensional parameters:

Rayleigh number:	$Ra = \alpha g d^3\Delta T/\kappa\nu$,
Coriolis number:	$\Omega = \omega d^2/\nu$,
Froude number:	$Fr = \omega^2 r_0/g$,
Prandtl number:	$\sigma = \nu/\kappa$,
aspect ratio:	$\gamma = r_0/d$.

The non-dimensional cylindrical domain is $(r, \theta, z) \in [0, \gamma]\times[0, 2\pi)\times[-1/2, 1/2]$. The resulting non-dimensional equations (from now on, $\boldsymbol{u}$ and T are dimensionless quantities) are

$$(\partial_t + \boldsymbol{u}\cdot\nabla)\boldsymbol{u} = -\nabla p + \sigma\nabla^2\boldsymbol{u} + \sigma Ra T\hat{z} + 2\sigma\Omega\boldsymbol{u}\times\hat{z} - \frac{\sigma Fr Ra}{\gamma}T\boldsymbol{r}, \tag{2.5}$$

$$(\partial_t + \boldsymbol{u}\cdot\nabla)T = \nabla^2 T, \tag{2.6}$$

$$\nabla\cdot\boldsymbol{u} = 0. \tag{2.7}$$

The boundary conditions for $\boldsymbol{u}$ and T are:

$$r = \gamma: \quad T_r = u = v = w = 0, \tag{2.8}$$

$$z = \pm\tfrac{1}{2}: \quad T = \mp 0.5,\ u = v = w = 0, \tag{2.9}$$

where (u, v, w) are the components of $\boldsymbol{u}$ in cylindrical coordinates. Regularity conditions (i.e. that the velocity and temperature be analytic) on the axis ($r = 0$) are enforced using appropriate spectral expansions for $\boldsymbol{u}$ and T.

In this study, we are interested in the EBF instability of the wall modes near onset of convection, and all the experiments on this topic have been conducted in the small centrifugal force limit. Hence, we take $Fr = 0$ here and shall present the effects of $Fr \neq 0$ elsewhere. Experiments on the onset of RRBC have typically been restricted to quite weak Coriolis force, as measured by Ω. This restriction is due to the desire to keep the centrifugal force small (i.e. restricting the Froude number $Fr < 0.01$), and so experiments have typically only explored the effects of a very limited amount of rotation. Here, we take $Fr = 0$ but use a large $\Omega = 625$ so that the wall modes dominate in $\epsilon = (Ra - Ra_C)/Ra_C \in [0, 1)$ for Prandtl number $\sigma = 7$ (essentially water) in a cylinder of moderate aspect ratio $\gamma = r_0/d = 4$.

The governing equations are invariant under rotations around the axis of the cylinder. If R_α is a rotation of angle α around the z-axis, its action is

$$R_\alpha(u, v, w, T, p)(r, \theta, z) = (u, v, w, T, p)(r, \theta + \alpha, z). \tag{2.10}$$

These rotations generate the symmetry group $SO(2)$. If the Froude number is zero, as in the present study, the governing equations are also invariant under reflection about the mid-plane, K_z, with action

$$K_z(u, v, w, T, p)(r, \theta, z) = (u, v, -w, -T, p)(r, \theta, -z). \tag{2.11}$$

This transformation generates the abstract group Z_2, and commutes with rotations. The complete symmetry group of the system is $SO(2) \times Z_2$.

2.1. *Numerical method*

The governing equations have been solved using the second-order time-splitting method proposed in Hughes & Randriamampianina (1998) combined with a pseudo-spectral method for the spatial discretization, using a Galerkin–Fourier expansion in the azimuthal coordinate θ and Chebyshev collocation in r and z. The radial dependence of the variables is approximated by a Chebyshev expansion between $-\gamma$ and γ and enforcing their proper parities at the origin (Fornberg 1998). Specifically, the scalar field T has even parity $T(-r, \theta, z) = T(r, \theta + \pi, z)$, as does the vertical velocity w, whereas u and v have odd parity. To avoid including the origin in the collocation mesh, an odd number of Gauss–Lobatto points in r is used and the equations are solved only in the interval $(0, \gamma]$. Following Orszag & Patera (1983), we have used the combinations $u_+ = u + \mathrm{i}v$ and $u_- = u - \mathrm{i}v$ in order to decouple the linear diffusion terms in the momentum equations. For each Fourier mode, the resulting Helmholtz equations for T, w, u_+ and u_- have been solved using a diagonalization technique in the two coordinates r and z. The imposed parity of the functions guarantees the regularity conditions at the origin required to solve the Helmholtz equations (Mercader, Net & Falqués 1991).

The code has been tested by comparing with results reported in Rüdiger & Feudel (2000), Marques & Lopez (2001), Lopez *et al.* (2002) and Rüdiger & Knobloch (2003). The agreement is excellent in all cases and the comparisons also reveal the high performance of the new code. Here, we have fixed $\gamma = 4$, $\sigma = 7.0$, $\Omega = 625$ and $Fr = 0$ and consider variations in Ra. We have used 24 spectral modes in z, 48 in r, a varying number of Fourier modes in θ, between 184 and 350, and a time step $\mathrm{d}t = 2 \times 10^{-5}$ thermal time units.

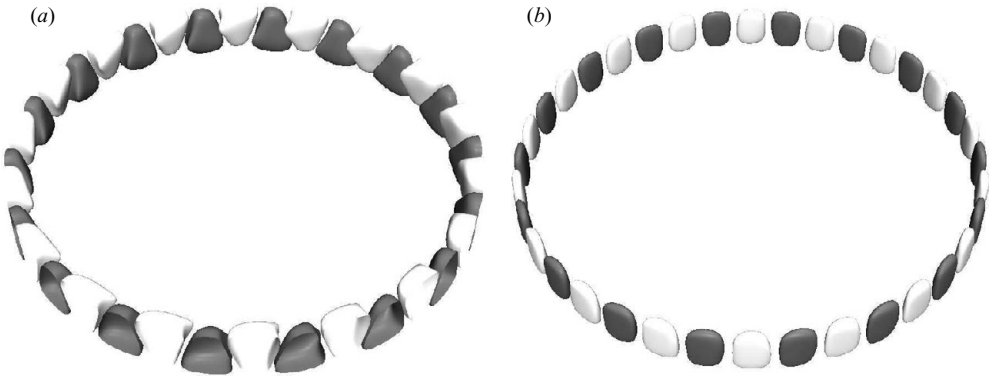

FIGURE 1. Isosurfaces of (a) temperature at $T = 0.025$ (light grey) and $T = -0.025$ (dark grey) and (b) vertical vorticity at levels 5 (light grey) and -5 (dark grey), of W_{18} at $Ra = 5 \times 10^4$, $\Omega = 625$, $\sigma = 7$ and $\gamma = 4$.

It is useful, in the time evolution and also in the linear stability analysis, to monitor the kinetic energy associated with each Fourier mode in the spectral approximation:

$$E_m(t) = \frac{1}{\gamma^2} \int_0^1 \int_0^\gamma \boldsymbol{u}_m^* \cdot \boldsymbol{u}_m \, r \, \mathrm{d}r \, \mathrm{d}z, \tag{2.12}$$

where * denotes complex conjugate and $\boldsymbol{u}_m$ is the m-Fourier component of the velocity field.

3. Results

3.1. *Hopf bifurcations to wall modes*

RRBC has $SO(2) \times Z_2$ symmetry, and the onset of the wall modes breaks both the $SO(2)$ and Z_2 symmetries. Breaking $SO(2)$ leads to a solution which is periodic in the azimuthal direction with wavenumber m; the corresponding symmetry group Z_m is generated by the azimuthal rotation $R_{2\pi/m}$. This solution W_m is a rotating wave (Ecke *et al.* 1992): it precesses such that in a frame of reference rotating with the precession frequency, the structure is stationary. Although the mid-plane reflection symmetry K_z is broken, the rotating wave still has a Z_2 symmetry: a roto-reflection whose action is a reflection about the mid-plane followed by an azimuthal rotation of half a period, $S_m = K_z R_{\pi/m}$. This symmetry can also be viewed as a spatio-temporal symmetry: a K_z reflection followed by a half-period advance in time. The action of this symmetry S_m is

$$\begin{aligned} S_m(u, v, w, T, p)(r, \theta, z, t) &= (u, v, -w, -T, p)(r, \theta + \pi/m, -z, t) \\ &= (u, v, -w, -T, p)(r, \theta, -z, t + \tau_m/2), \end{aligned} \tag{3.1}$$

where τ_m is the precession period of W_m, defined as the time necessary for the pattern to repeat, corresponding to a rotation of $2\pi/m$. The symmetry group of the rotating wave is $Z_m \times Z_2$. The structure of a typical wall mode with azimuthal wavenumber $m = 18$, W_{18}, at $Ra = 5 \times 10^4$, $\Omega = 625$, $\sigma = 7$ and $\gamma = 4$ is shown in figure 1. Figure 1(a) shows isosurfaces of the temperature at $T = 0.025$ (light grey) and $T = -0.025$ (dark grey) and figure 1(b) shows isosurfaces of the vertical component of vorticity at levels 5 (light grey) and -5 (dark grey). The figure illustrates for a typical wall mode that the convection is restricted to a thin boundary-layer region and is comprised of rising and descending hot and cold swirling thermals. Figure 2 shows

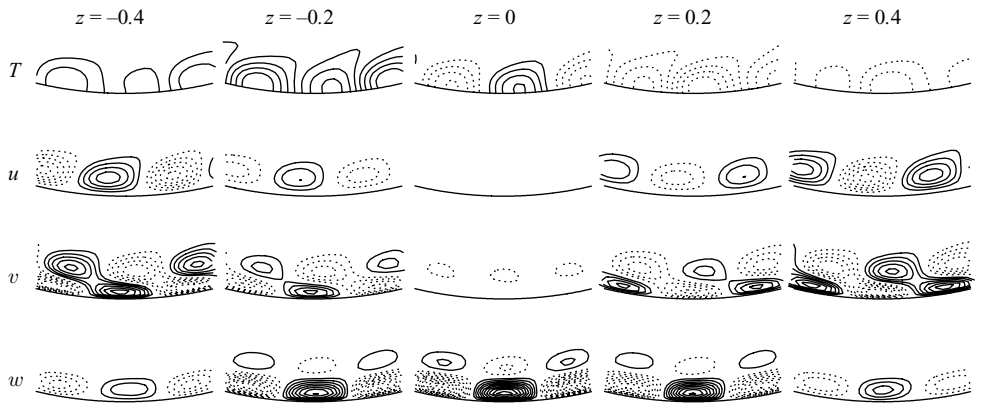

FIGURE 2. Contours of T, u, v and w near the cylinder wall over $\theta \in (0, \pi/6]$ at various depths as indicated of W_{18} at $Ra = 5 \times 10^4$, $\Omega = 625$, $\sigma = 7$, and $\gamma = 4$. There are 12 linearly spaced contours in the intervals $[-0.5, 0.5]$ for T and $[-20, 20]$ for the velocities; solid (dashed) lines indicate positive (negative) contour levels.

close-up views of the wall region for $\theta \in [0, \pi/6]$, presenting contour plots of the temperature and the three components of velocity for a pair of thermals at various depths. These figures show the Z_2 symmetry in z, generated by the roto-reflection $S_m = K_z R_{\pi/m}$, and the Z_m symmetry in θ, generated by the rotation $R_{2\pi/m}$, of the wall modes. It is useful to specify the symmetries of each of the Fourier components of W_m. Let us focus on the temperature $T^{(m)}$ of W_m (analogous equations can be obtained for the velocity field), and let $T^{(m)}_{j\,m}$ be its Fourier components:

$$T^{(m)}(r, \theta, z) = \sum_{j=-\infty}^{\infty} T^{(m)}_{j\,m}(r, z) \mathrm{e}^{\mathrm{i}\,j\,m\,\theta}. \tag{3.2}$$

The invariance of W_m to the S_m symmetry results in

$$T^{(m)}_{j\,m}(r, z) = (-1)^{j+1} T^{(m)}_{j\,m}(r, -z), \tag{3.3}$$

i.e. the odd (even) harmonics of m are even (odd) functions of z.

As noted experimentally (Ning & Ecke 1993; Liu & Ecke 1997, 1999), the wall mode is essentially a one-dimensional pattern, characterized by the wavenumber m. From now on, we shall describe changes in the structure of wall mode solutions as Ra is varied in terms of m and illustrate these using T at the mid-height $z = 0$.

The bifurcation from the basic state to wall modes is a Hopf bifurcation and for RRBC it is typically supercritical. Figure 3 shows the marginal stability curve (•) for the Hopf bifurcation from the base state to rotating waves with different azimuthal wavenumbers $m \in [8, 38]$. The curve has a minimum at $m_c = 18$, $Ra_c \approx 42\,286$. The marginal stability curve has been found by evolution of the linearized governing equations taking as initial condition the base state plus a perturbation in the mth azimuthal Fourier mode. Monitoring the growth rate of the mode m kinetic energy, the real part of the most dangerous eigenvalue is computed, and the bifurcation point on the marginal curve corresponds to zero growth rate. The precession frequencies ω_c of the bifurcated solutions on the marginal curve are plotted as a function of m in figure 4. The results obtained here are consistent with Goldstein *et al.* (1993), although the linear instability of the base flow for the parameter values considered here was not included in that paper.

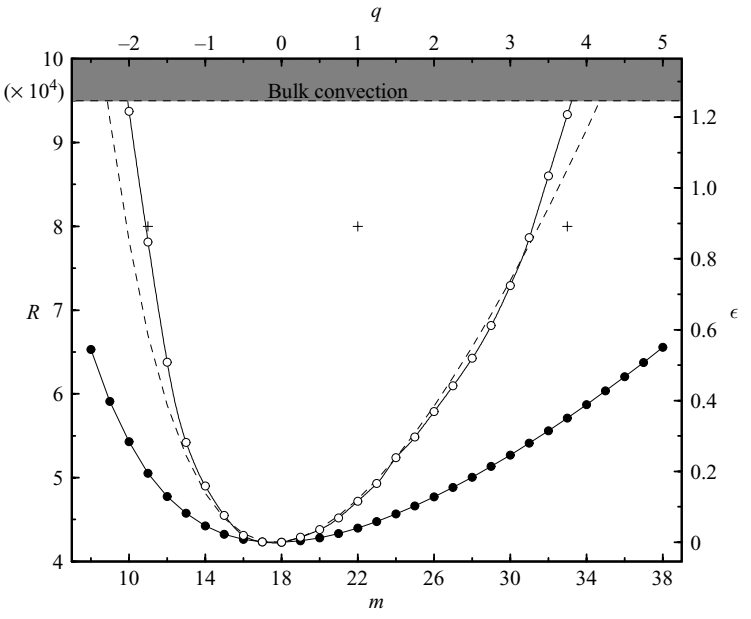

FIGURE 3. Stability diagram for wall modes W_m with azimuthal wavenumber $m \in [8, 38]$, showing the marginal stability curve (•) and the Eckhaus–Benjamin–Feir curve (○), for $\Omega = 625$, $\sigma = 7$, $\gamma = 4$. The curves are shown both in terms of (m, Ra) and the scaled variables $(\epsilon = (Ra - Ra_c)/Ra_c,\ q = (m - m_c)/\gamma)$. The dotted curve is the classic prediction for the EBF curve, given by $\epsilon = 3\epsilon_M$ where $\epsilon_M(q)$ is the marginal stability curve.

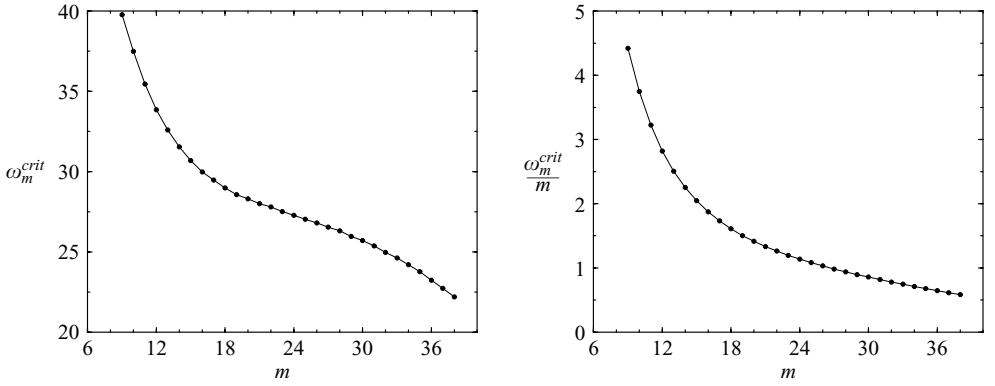

FIGURE 4. (*a*) Critical frequencies ω_m^{crit} of the bifurcating wall modes on the marginal curve as a function of m and (*b*) the ratio ω_m^{crit}/m.

For moderate to large γ ($\gamma = 4$ certainly fits this), there are many wall modes that bifurcate directly from the conduction state for small $\epsilon = (Ra - Ra_c)/Ra_c$. Varying γ changes which wall mode is first to bifurcate from the conduction state. The onset can be viewed as a mode competition between wall modes with $m = n$ and $m = n + 1$. It appears that near onset, this competition is organized by a double Hopf bifurcation of the simplest type (Kuznetsov 1998), where in a region of (Ra, γ)-space, the two wall modes coexist and are stable, and the mixed mode between them is unstable. This region is bounded by secondary Hopf bifurcations, where the wall modes undergo

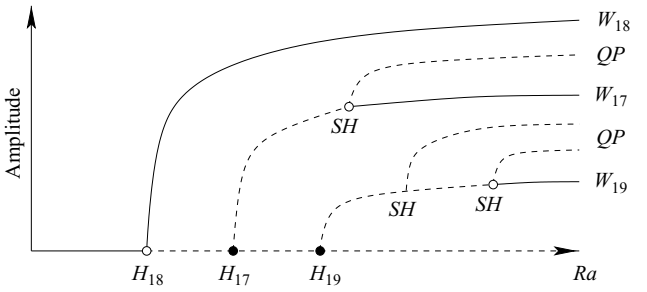

FIGURE 5. Schematic of the secondary Hopf bifurcations (SH) that stabilize the unstable wall modes. Solid (dashed) lines are stable (unstable) solutions. The horizontal axis is the Rayleigh number Ra and the vertical axis is a measure of the pure and mixed-mode wall modes (an amplitude). The conductive state has zero amplitude and coincides with the Ra axis. The wall modes appear at Hopf bifurcations H_m, where m is the azimuthal wavenumber of the corresponding wall mode (•, same as in figure 3). QP are quasi-periodic mixed-mode solutions born at the secondary Hopf bifurcations SH. The wall modes change stability at the circle points (○, as in figure 3).

bifurcations to the mixed mode. Note that this secondary Hopf bifurcation is not the Neimark–Sacker bifurcation found in generic double Hopf bifurcations because in this case the limit cycles are special, they are rotating waves or relative equilibria, and so one should not expect to find any resonance behaviour associated with the resulting mixed mode (Rand 1982; Krupa 1990; Knobloch 1994). Further, the double Hopf bifurcation itself can only be resonant if $n/(n+1) = \omega_n^{crit}/\omega_{n+1}^{crit}$ where ω_n^{crit} and ω_{n+1}^{crit} are the precession frequencies on the marginal curve (Marques, Lopez & Shen 2002), and this is not found to be the case in our problem, as can be seen from figure 4(*b*); for resonance there must be two values of m with the same value of ω_m^{crit}/m, which is not the case for the aspect ratio $\gamma = 4$ considered here.

The mixed modes not only exist between successive integer values of m, but in fact for other values as well. For example, from figure 3 we see that W_{12} and W_{26} bifurcate from the base state at almost the same Rayleigh number ($Ra = 47\,737$ and 47 690, respectively); a small change in γ will result in the corresponding double Hopf bifurcation and the associated mixed mode. All these wall modes and mixed modes are unstable at onset, except for the critical wall mode ($m_c = 18$ for the $\gamma = 4$ case studied here). However, for $\gamma > 1$, a large number of wall modes are stable for moderate values of ϵ. In our numerical problem with $\gamma = 4$ and $\Omega = 625$, stable wall modes exist with $m \in [10, 33]$ (see figure 3, inside the EBF curve, shown as the solid line with symbols ○). We have extended the computations up to the onset of bulk convection, at about $Ra \approx 95\,000$, which destabilizes the wall modes. Increasing Ra beyond this level does not produce additional stable wall modes. Liu & Ecke (1999) report $m \in [17, 32]$ in experiments with $\gamma = 5$ and $\Omega = 274$. If all of these wall modes originally bifurcate from the conduction state, all but one are unstable when they are created and must undergo a number of secondary bifurcations in order to become stable. These secondary bifurcations are the secondary Hopf bifurcations where the mixed modes are born; these secondary Hopf bifurcations reduce the number of eigenvalues with modulus greater than one, so the initially unstable wall modes become stable after a number of secondary Hopf bifurcations (figure 5). See Tuckerman & Barkley (1990) for an analogous situation in the Ginzburg–Landau equation with Z_2 symmetry, where pitchfork bifurcations take the place of the Hopf bifurcations here.

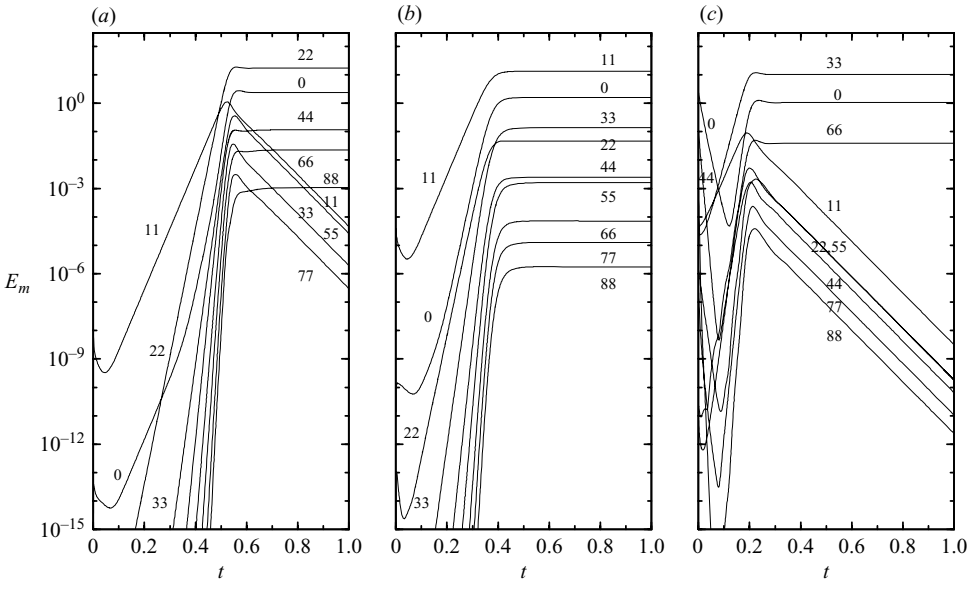

FIGURE 6. Modal kinetic energy E_m as a function of time for $Ra = 8.0 \times 10^4$, starting from rest with perturbation in the $m = 11$ azimuthal Fourier mode; (*a*) computing in the 11-Fourier subspace; (*b*) computing in the 11-roto-reflection subspace; and (*c*) computing in the 11-roto-reflection subspace but with a convoluted initial condition (see text for details). The labels on the curves refer to the azimuthal wavenumber m.

3.2. *Eckhaus–Benjamin–Feir bifurcations of wall modes*

Figure 3 includes the Eckhaus–Benjamin–Feir (EBF) stability curve (solid line with symbols ○), where the various wall modes born on the marginal stability curve become stable with increasing Ra following a number of secondary bifurcations. We have obtained this curve by starting with a stable wall mode W_m at high enough Ra, and quasi-statically decreasing Ra until it becomes unstable and evolves either toward the base state or to a different wall mode. This results in an estimate of the EBF curve in (m, Ra). In order to compute the bifurcation point precisely, a linear stability analysis is performed, computing the growth rate of perturbations with different m values and using bisection in Ra until the bifurcation point is reached. This method works well except for the extreme values of m where the EBF curve has a large slope and mode competition plays a critical role.

In order to compute a wall mode with a given m, a sufficiently large value of Ra is selected and the time evolution code is initiated with the conductive state plus a random perturbation in the mth azimuthal Fourier mode. For small values of m, wall modes with some harmonics of m (typically W_{2m} and W_{3m}) are also stable, so they compete and can become dominant, resulting in an evolution to a wall mode with a wavenumber different from that desired. This is illustrated in figure 6(*a*) for $m = 11$ and $Ra = 8.0 \times 10^4$, showing that with a random perturbation in the $m = 11$ Fourier mode, the $m = 22$ Fourier mode is also excited, grows faster, and when it saturates nonlinearly, kills the $m = 11$ mode. This is a type of 1:2 resonance mechanism. Working in the m-Fourier subspace (i.e. only allowing Fourier modes that are multiples of m) is not sufficient to obtain W_m. Fortunately, we can use the roto-reflection Z_2 symmetry to reduce the subspace further. Because of this symmetry, a pure W_m only has Fourier modes that satisfy (3.3). Restricting computations to the roto-reflection subspace, the

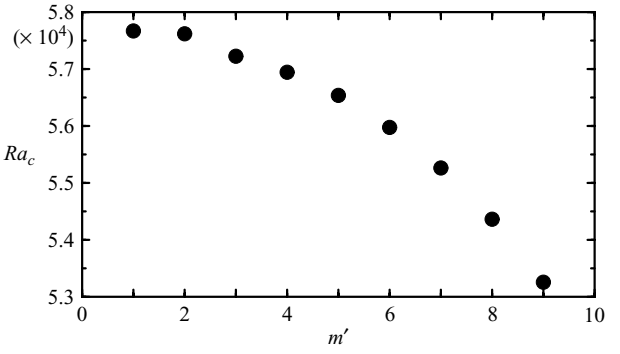

FIGURE 7. Critical Rayleigh numbers Ra_c of W_{26} wall mode for different perturbations m'. The W_{26} is stable for $Ra > 5.77 \times 10^4$.

competition with the W_{2m} is avoided, as can be seen in figure 6(*b*) for $m = 11$. The reason is that $T_{2m}^{(m)}$ and $T_{2m}^{(2m)}$ have opposite parity (3.3), so $T_{2m}^{(2m)}$ do not belong to the S_m roto-reflection subspace and it is not excited. However, the 1:3 mode competition with W_{3m} is still present ($T_{3m}^{(m)}$ and $T_{3m}^{(3m)}$ have the same parity), and depending on the initial conditions, the simulation can evolve to W_{3m} (figure 6*c*): here the initial condition is a transient state computed without any restriction, in which the dominant mode is $m = 44$, but $m = 11$ and $m = 33$ have almost the same weight; when restricted to the roto-reflection subspace, $m = 33$ becomes dominant. The wall modes W_{11}, W_{22} and W_{33} have been marked as + in figure 3; note that the W_{33} is unstable to general perturbations, but we have found that it is stable both in the $m = 11$ Fourier subspace and in the $m = 11$ roto-reflection subspace. As we have seen, for small m values it is difficult to compute stable wall modes, and without using appropriate initial conditions and restrictions to suitable symmetric subspaces, an apparent sharp cutoff in the EBF curve would be observed. In an experiment, it is typically not possible to restrict the flow to symmetric subspaces, and so we can expect to observe an apparent cutoff at low m values. Summarizing, the basin of attraction of the wall modes with small m is apparently very narrow, and when computing these W_m with a time evolution code (or obtaining them in an experiment), simple approaches will fail, and a convoluted approach is required: working in convenient symmetric subspaces and using appropriate initial conditions.

Once the wall modes have been obtained (by computing in appropriate subspaces), their stability to arbitrary perturbations is then determined. A linear stability analysis of W_m is performed using the nonlinear evolution code with W_m plus perturbations as initial conditions by determining the growth rates of perturbations with different azimuthal wavenumbers $m' \neq m$. In fact, it is sufficient to consider perturbations with $m' \in [1, m/2]$ since, as a result of the coupling between the perturbation and the Fourier modes of W_m in the linearized equations for the perturbations, the perturbations with azimuthal wavenumbers $j\,m \pm m'$, j an integer, are also excited. For given m and m', Ra is varied by bisection until the critical Ra corresponding to zero growth rate is determined. As a result the EBF curve is obtained. Although on the EBF curve only one of the perturbations becomes critical, resulting in a critical m_c' value, we have observed that perturbations with different m' values bifurcate very close to the EBF curve. For example, the most dangerous m' values and the corresponding critical Ra for W_{26} are shown in figure 7. When the m_c' perturbation saturates nonlinearly, the resulting wall mode can be not only any of the $W_{j\,m \pm m_c'}$,

j an integer, but also any of the $W_{j\,m\pm j'm_c'}$ with j and j' integers, because the nonlinear interactions excite these additional modes. Which one of all these possible wall modes results is determined by the nonlinear interactions and initial conditions. Moreover, there are additional $W_{m'}$ states bifurcating very close to the EBF curve that can also be excited by the nonlinear terms. Consequently, the azimuthal wavenumber of the resulting wall mode can be, and in many cases is, very different from the most dangerous m_c' value. Examples of nonlinear evolutions that result from crossing the EBF curve are presented in § 3.4.

There have been many theoretical and numerical studies of the 1:2 and 1:3 resonances in steady two-dimensional Rayleigh–Bénard convection (e.g. Mizushima & Fujimura 1992; Nagata 1995; Prat, Mercader & Knobloch 1998; Porter & Knobloch 2000). These are spatial resonances between steady-state bifurcations. In the case of RRBC, the bifurcations are not steady, they are of Hopf type. In order for the resonances to play a dynamical role, it is necessary for the ratio of the critical temporal frequencies to be equal to the ratio of the spatial wavenumbers. Assuming that this is the case for some particular parameter values, then the resonant normal forms for RRBC are the same as for steady two-dimensional Rayleigh–Bénard convection, but with complex coefficients. In particular, owing to the reflection symmetry of the governing equations and base state, resonances such as 1:3 in which the two modes have the same (odd) parity, have resonant terms of lower order than resonances such as 1:2 with different parities (one odd and the other even). The resonant terms in the 1:3 resonance are third order, whereas in the 1:2 resonance they are fifth order (Prat *et al.* 1998). Close to the bifurcation point (the marginal stability curve in figure 3) these differences can be important, and tend to favour resonances such as 1:3 compared to the 1:2. However, the wall modes become stable at the EBF curve, which is far away from the marginal stability curve (except for W_m with m very close to $m_c = 18$), where the nonlinear interactions are strong and the normal form analysis is no longer valid. This is clearly illustrated in figure 6, where the 1:2 resonance mechanism is easily excited, whereas the 1:3 resonance requires special initial conditions in order to become dominant.

Figure 3 also includes the (dotted line) curve $Ra(m) = Ra_c + 3(Ra_M(m) - Ra_c)$, where $Ra_M(m)$ is the marginal stability curve. This corresponds to the classic EBF prediction from the one-dimensional Ginzburg–Landau equation with cubic nonlinearity, $\epsilon = 3\epsilon_M$ where $\epsilon_M(q)$ is the marginal stability curve, $\epsilon = (Ra - Ra_c)/Ra_c$ and $q = (m - m_c)/\gamma$. It is evident that the EBF curve is not symmetric about $q = 0$; this is due to the marginal stability curve not being symmetric about $q = 0$ either. The marginal stability curve is only expected to be parabolic for Ra very close to Ra_c. Also, the actual EBF curve is predicted quite well by the classic Ginzburg–Landau estimate, although it lies to slightly higher Ra. The experimental results of Liu & Ecke (1999) are also at Ra values slightly higher than the classic prediction for EBF.

Of course, although we talk about curves, both the marginal stability curve and the Eckhaus curve are in fact loci of discrete points since the azimuthal wavenumber m is an integer. According to Tuckerman & Barkley (1990), for small ϵ the loci of Eckhaus points should fall on a parabolic curve and intersect the marginal stability curve near the minimum. For small ϵ, this is approximately the case, but there are obvious asymmetries for large ϵ between the small-m and large-m modes. For Ra above the Eckhaus curve, several stable wall modes coexist and the transitions between these modes when crossing the Eckhaus curve from above are explored in some detail in the following sections.

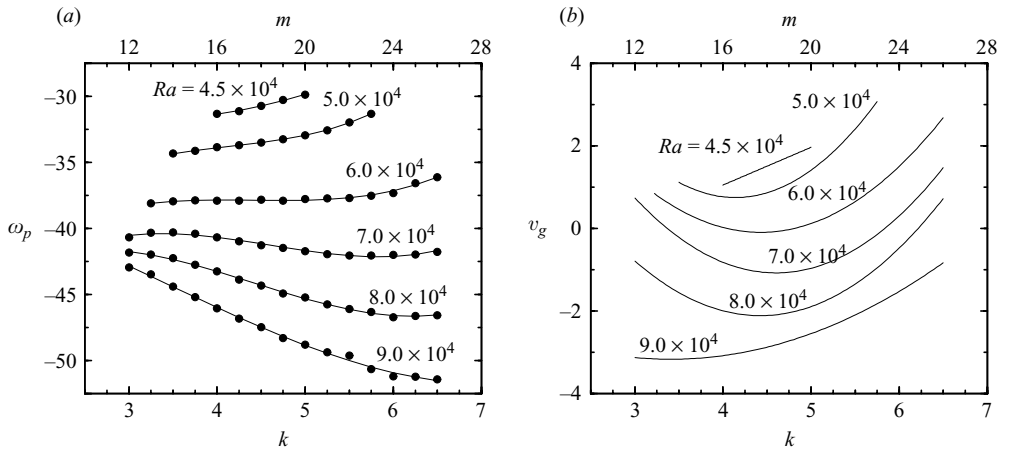

FIGURE 8. (*a*) Dispersion relation curves $\omega_p(k)$ and (*b*) the corresponding group velocities $v_g(k)$ for the EBF-stable wall modes at $\Omega = 625$, $\sigma = 7$, $\gamma = 4$ and various Ra as indicated. Cubic line fits have been used in $\omega_p(k)$ (except for the smallest Ra case for which a quadratic fit has been used), and $v_g(k)$ curves are obtained by differentiation of these fits.

3.3. *Characteristics of the EBF-stable wall modes*

Figure 8(*a*) shows the variation of the precession frequency ω_p with the azimuthal wavenumber m for different values of Ra. The precession frequency increases with increasing Ra, and at a given Ra it varies nonlinearly with the wavenumber. To obtain the nonlinear dispersion relation, $\omega_p(k)$, we use the scaled wavenumber $k = m/\gamma$, corresponding to a wavelength $\lambda = 2\pi d/k = 2\pi r_0/m$, as introduced in Ning & Ecke (1993), and the precession frequency is negative since the wall modes precess retrograde with respect to the imposed rotation of the container. From $\omega_p(k)$, the corresponding group velocity $v_g = \partial\omega_p/\partial k$, shown in figure 8(*b*), is obtained. Since $\omega_p(k)$ is defined for a discrete set of k values corresponding to integer m, we have numerically computed this derivative using a cubic fit to $\omega_p(k)$, shown as solid lines in figure 8(*a*), and taking the corresponding derivative; hence the v_g curves for fixed Ra shown in the figure are parabolic fits. The exception is the $Ra = 4.5 \times 10^4$ case, which is close to the minimum of the Eckhaus curve, where a linear estimate is used, from a parabolic fit to $\omega_p(k)$. In fact, dispersion relations obtained from complex Ginzburg–Landau equation models with cubic nonlinearities (the significant nonlinearities close to the bifurcation point) always produce linear group velocities. Higher-order terms must be introduced to account for the experimentally observed deviations from linearity (Liu & Ecke 1999); the use of quintic terms results in a quadratic dependence of v_g on k. Our numerical results suggest that deviations from Ginzburg–Landau with cubic nonlinearities occur for moderate values of the criticality ϵ. The quadratic fits in figure 8(*b*) are in excellent agreement with the experimental results of Liu & Ecke (1999), see their figure 26(*b*). They considered ϵ up to 0.26; for these small ϵ, v_g is positive. However, for $\epsilon > 0.42$ (corresponding to $Ra > 6 \times 10^4$), we find that v_g becomes negative.

The heat transport efficiency of the different wall modes is analysed in figure 9(*a*), where the increase in Nusselt number with respect to the conductive state, $Nu - 1$, is plotted against Ra. The maximum efficiency corresponds to the modes that bifurcate first from the base state, W_{18} and W_{17}, but the differences are small. Comparing the Nusselt number of modes $m_c \pm j$, small modes $(m_c - j)$ are more efficient than

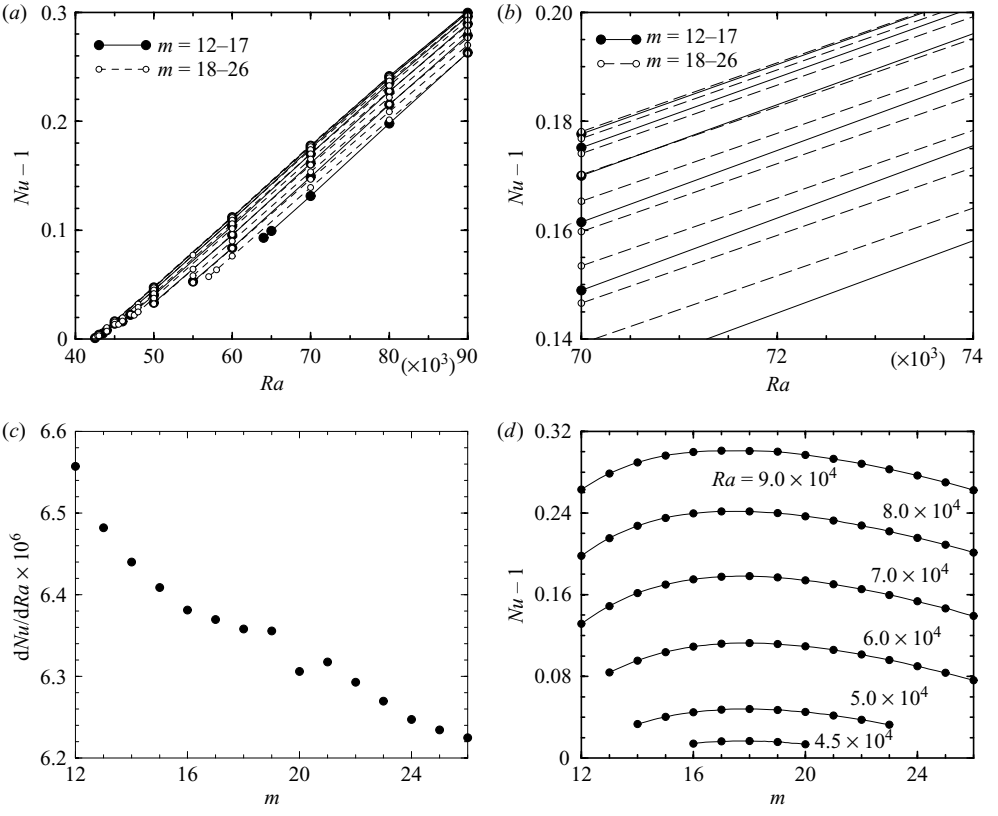

FIGURE 9. Variation of (*a*) $Nu-1$ with Ra, where the low-m ($m \in [12, 17]$) results are plotted with solid lines and filled symbols and Nu increases with m for these, and the high-m ($m \in [18, 26]$) results are plotted with dashed lines and open symbols and Nu decreases with increasing m for these; (*b*) an enlargement of part of (*a*); (*c*) $\partial Nu/\partial Ra$ with m; and (*d*) $Nu-1$ with m for the stable wall modes inside the Eckhaus–Benjamin–Feir curve in figure 3.

large modes ($m_c + j$) for $j \leqslant 3$, close to the critical $m_c = 18$, and for $j > 3$ it is the opposite: large modes are more efficient in transporting heat. This is readily apparent from figure 9(*b*). Moreover, $Nu-1$ varies linearly with Ra, and the slope $\partial Nu/\partial Ra$ is approximately independent of m; varying by no more than about 5% over a wide range of wavenumbers $m \in [12, 26]$ (see figure 9*c*). This behaviour has also been observed experimentally, where it has been further noted that the slope is also approximately independent of Ω in a cylinder of aspect ratio $\gamma = 5$ (Liu & Ecke 1999, figure 6). Figure 9(*d*) shows the variation of $Nu-1$ with m for various Ra. For small ϵ, W_{18} transports the maximum heat and the maximum shifts ever so slightly to W_{17} as ϵ, i.e. Ra, increases. Notice, however, that the $Nu(m)$ relationship becomes more skewed as Ra is increased.

3.4. *Dynamics of the EBF transition*

The EBF instability is observed by using a wall mode W_m with $m \neq m_c$ at some Ra above the EBF curve as an initial condition for an evolution with Ra below the EBF curve. Below the EBF curve, this wall mode is unstable and the subsequent evolution involves either the annihilation or the creation of a number of the cold/hot wall plume pairs to a new wall mode with different m. The wall plume pairs will be annihilated

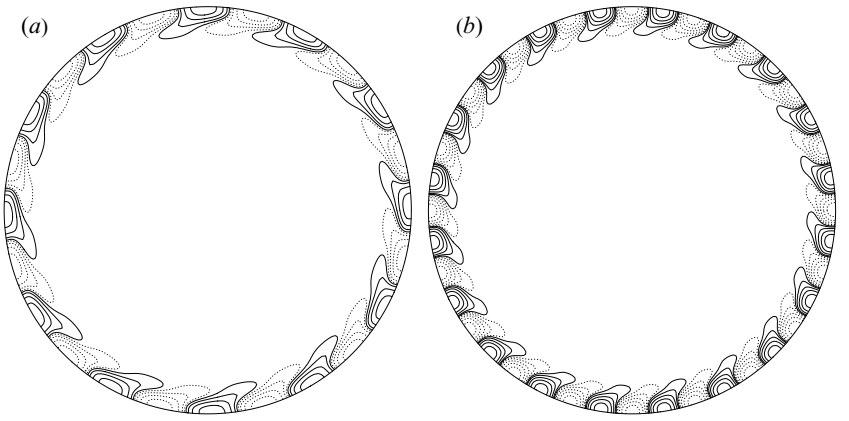

FIGURE 10. Contours of T at $z = 0$ of (*a*) W_{12} at $Ra = 6.5 \times 10^4$ and (*b*) W_{20} at $Ra = 5.0 \times 10^4$.

or created, depending on whether m is greater than or less than m_c. The wall mode becomes EBF unstable via a secondary Hopf bifurcation; the quasi-periodic state which is spawned at that bifurcation is unstable and not observed directly. At the lower Ra, there are still a number of wall modes with different m that are stable. However, it is difficult to predict to which the flow will evolve as their basins of attraction are complicated to compute and the final evolution is dependent on initial conditions. Typically, we have found that the change in the wavenumber on crossing the EBF curve is greater than one, and the final $m \geqslant m_c$ even with initial $m < m_c$. We shall now illustrate a number of typical transitions we have observed.

Figure 10 shows the initial W_{12} at $Ra = 6.5 \times 10^4$ and the final W_{20} following a reduction of Ra to 5.0×10^4. From figure 3, we see that at 5.0×10^4, both W_{12} and W_{13} are below the EBF curve, but that W_m with $m \in [14, 23]$ are all EBF stable. Following the reduction in Ra, there was a long transient during which the $m = 20$ mode grew exponentially and saturated nonlinearly about 3 thermal time units after the reduction in Ra. At that time, over a short period (about 0.2 thermal time units) and almost simultaneously, a number of hot and cold wall plumes split to produce W_{20} shown in figure 10(*b*). A convenient way of illustrating the evolution is a space–time plot of T at mid-height $z = 0$ and very near the cylinder wall at $r = 0.95\gamma$ (figure 11). The dark (light) contours correspond to $T < 0$ (>0). The vertical axis is the azimuthal angle θ and the horizontal axis is time in thermal time units. The constant negative slope of the T-pattern indicates the constant precession retrograde to the rotation of the cylinder of the initial W_{12} mode. Following the splitting of the wall plumes at $t \approx 2.5$, the newly formed W_{20} also precesses steadily and retrograde, but at a noticeably slower rate. Figure 12 shows the corresponding evolution of the Nusselt number; W_{12} is inefficient at $Ra = 5.0 \times 10^4$, but as W_{20} saturates, Nu shoots up over the time $t \approx 2.4$ to 2.8 and then quickly saturates to a constant. The initial state had $m = 12$ and the final state has $m = 20 > m_c = 18$, and Nu for W_{18} is greater than for W_{20} (see figure 9*d*). Liu & Ecke (1999) note that in their experiments they never observed a transition that reduced (increased) m beyond m_c when starting from higher (lower) m, but that, in principle, the bound for the transition might be the m at the opposite end of the EBF stable band for the particular Ra.

Figure 13 shows two more transitions across the EBF curve starting with $m < m_c$. Figure 13(*a*) started with W_{13} at $Ra = 5.5 \times 10^4$, and reducing Ra to 5.0×10^4 precipitated a transition to W_{18}. In this case, the splitting of the wall plumes did

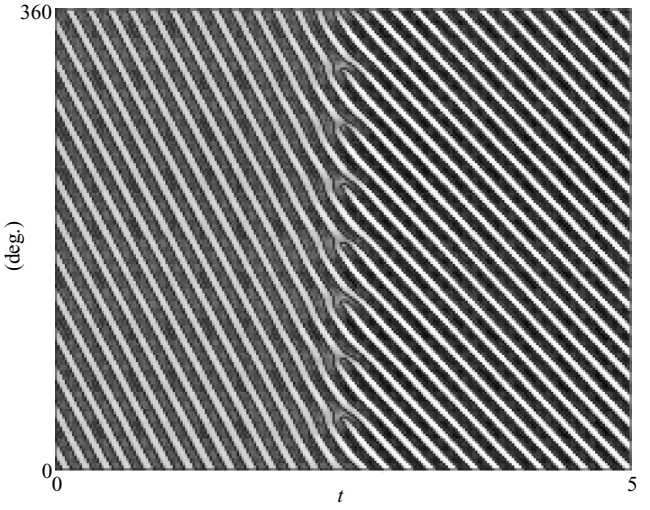

FIGURE 11. Angle-time plots of the temperature at mid-height $z = 0$ close to the wall at $r = 0.95\gamma$, starting from W_{12} at $Ra = 6.5 \times 10^4$ and reducing Ra to 5.0×10^4.

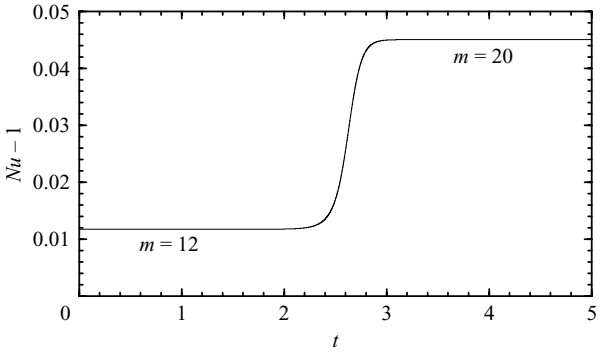

FIGURE 12. Time variation of the Nusselt number for the transition shown in figure 11.

not occur simultaneously, but rather was spread over almost one thermal time unit. The corresponding evolution of the Nusselt number (figure 14) shows the associated non-smoothness of this transition. On the other hand, in figures 13(*b*) and 14 we find that the transition from W_{14} at $Ra = 5.0 \times 10^4$ to W_{18} following a reduction to $Ra = 4.5 \times 10^4$ is smooth and occurred with almost simultaneous splitting of the wall plumes.

We now consider some transitions starting from wall modes with $m > m_c$. The transition from W_{22} at $Ra = 5.0 \times 10^4$ following a reduction to $Ra = 4.5 \times 10^4$ is shown in figures 15(*a*) and 16. At $Ra = 4.5 \times 10^4$, W_{21} is just EBF stable; the EBF stable band at this Ra is $m \in [16, 21]$. As in the transitions with the initial $m < m_c$ discussed above, this transition also has a very slow transient. In fact, the transient before any transition is evident is twice as long. By $t \approx 5$, there are a number of wall plumes that are annihilated over a period of about two thermal times, and while these annihilations do not occur simultaneously, the associated Nusselt number development is smooth and by a little beyond $t = 6$, Nu is constant and W_{18} has

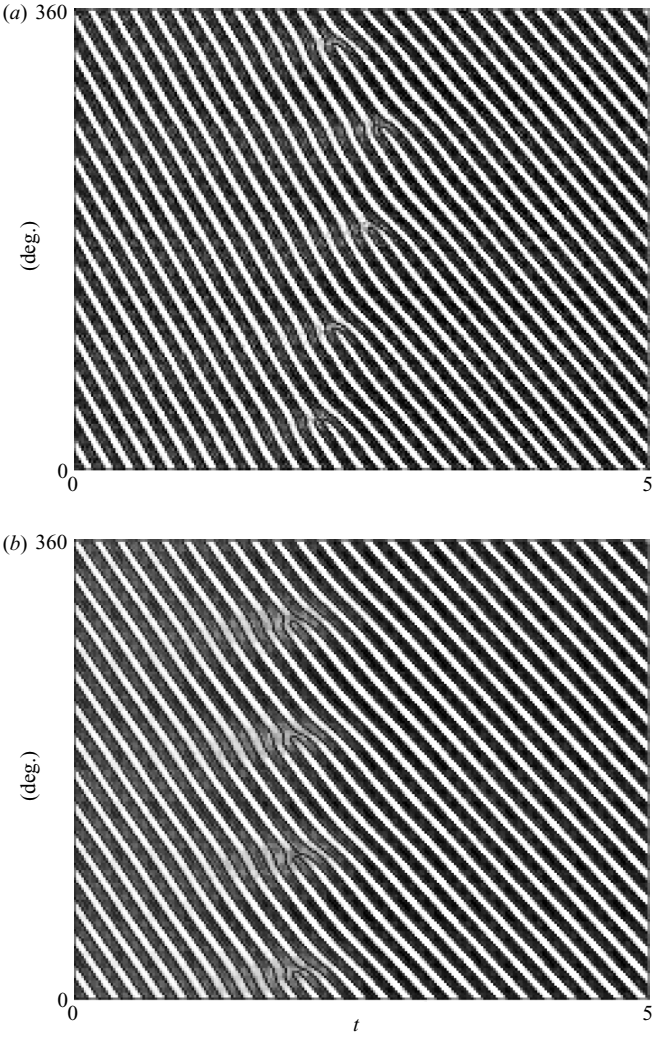

FIGURE 13. Angle-time plots of the temperature at mid-height $z = 0$ close to the wall at $r = 0.95\gamma$. (*a*) Starting from W_{13} at $Ra = 5.5 \times 10^4$ reducing to $Ra = 5.0 \times 10^4$, and (*b*) starting from W_{14} at $Ra = 5.0 \times 10^4$ reducing to $Ra = 4.5 \times 10^4$.

established itself and is precessing steadily retrograde at a faster rate than W_{22} from which it transitioned.

A transition from W_{23} at $Ra = 5.0 \times 10^4$ following a reduction to $Ra = 4.5 \times 10^4$ is shown in figures 15(*b*) and 16. In this case, the initial evolution is very rapid with a pair of hot plumes and the in between cold plume being annihilated to leave a single hot plume within one thermal time unit, resulting in W_{22} mode. However, at $Ra = 4.5 \times 10^4$ this mode is also EBF unstable and more plumes are annihilated after about another thermal time unit to produce W_{21}, which is also EBF unstable. By $t \approx 4$, two more annihilations occur almost simultaneously and about 160° apart azimuthally, resulting in W_{19}. Although W_{19} is well within the EBF stable band at this Ra, the subsequent evolution is a slow re-adjustment of the wall plumes. A close examination of the space–time plot (figure 15*b*) shows that even at $t = 10$ the solution

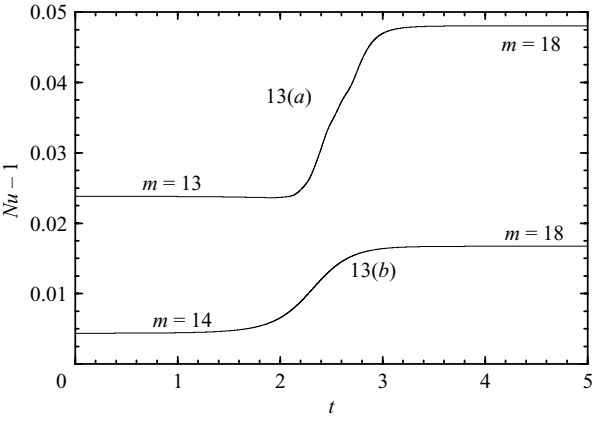

FIGURE 14. Time variation of the Nusselt number for the transitions shown in figure 13.

is still not precessing steadily. This is also evident in the Nu time-series plot (figure 16) which shows that Nu has still not reached a steady state by $t = 10$, but it does seem to be asymptoting to one.

The transition shown in figures 15(c) and 16 from W_{24} at $Ra = 5.5 \times 10^4$ following a reduction to $Ra = 5.0 \times 10^4$ shows an even slower adjustment than the previous case. At $Ra = 5.0 \times 10^4$, W_{23} is EBF stable. The initial evolution shows a single annihilation event at $t \approx 2$ to W_{23}, followed by a second annihilation event at about $t = 3$ to W_{22}. The subsequent evolution has been computed out to $t = 10$, but it has not settled down to W_{22} with a constant precession. The space–time plot shows that half of the wall plumes are precessing slightly faster than the rest, and that this fast precessing band is drifting prograde (in the positive θ-direction). The corresponding Nu time-series plot shows that Nu is still not constant by $t = 10$, and it is not clear whether this very slow transient will eventually asymptote to a constant or if there will be another annihilation event at some later time.

This type of very slow adjustments following a crossing of the EBF curve has also been observed experimentally by Liu & Ecke (1999), where they considered in detail the associated phase dynamics (the phase being the spatial gradient of the pattern wavenumber) and showed that higher-order generalizations to the complex Ginzburg–Landau equation are required to account for the observed slow phase dynamics. That these types of slow phase dynamics also occur in the numerical simulations suggests that they are inherent to the problem and not due to slow drifts in experimental conditions over the long durations of the experiments.

4. Conclusions

The EBF instability in rotating convection has been analysed using direct numerical simulations of the Navier–Stokes equations in the Boussinesq approximation. Comparisons with the experimental results of Liu & Ecke (1999) are excellent, and our numerical results have extended far beyond the onset of convection with $\epsilon = (Ra - Ra_c)/Ra_c$ more than twice as large as in the experiments and to larger Coriolis force, as measured by $\Omega = \omega d^2/\nu$. In fact, we have extended the computations up to the onset of bulk convection (at about $Ra \approx 95\,000$) that destabilizes the wall modes, resulting in much more complex flows, including Küppers-Lortz-type dynamics. We have computed the EBF curve, and several properties of the bifurcated

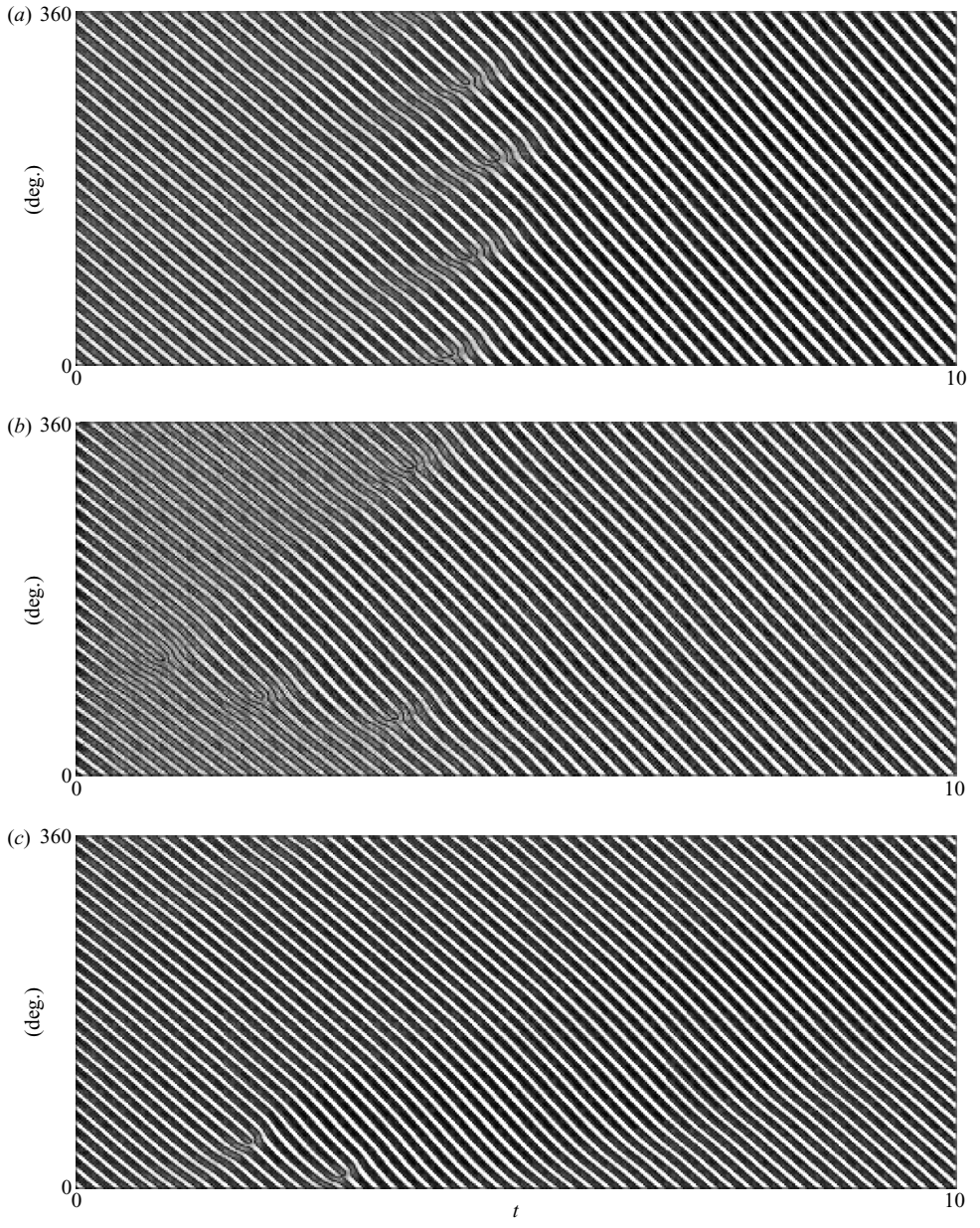

FIGURE 15. Angle–time plots of the temperature at mid-height $z = 0$ close to the wall at $r = 0.95\gamma$. (*a*) Starting from W_{22} at $Ra = 5.0 \times 10^4$ reducing to $Ra = 4.5 \times 10^4$, (*b*) starting from W_{23} at $Ra = 5.0 \times 10^4$ reducing to $Ra = 4.5 \times 10^4$, (*c*) starting from W_{24} at $Ra = 5.5 \times 10^4$ reducing to $Ra = 5.0 \times 10^4$.

rotating waves: the precession periods, the dispersion relation curves $\omega_p(k)$, the group velocities, the variation of the Nusselt number with Ra and m, and the phase dynamics associated with transitions across the EBF curve. These results are consistent with the experimentally observed trends at lower ϵ and Ω. Furthermore, an apparent cutoff of the EBF instability at low wavenumbers owing to a resonance with harmonics has been found, and the true EBF curve was determined by first computing the wall

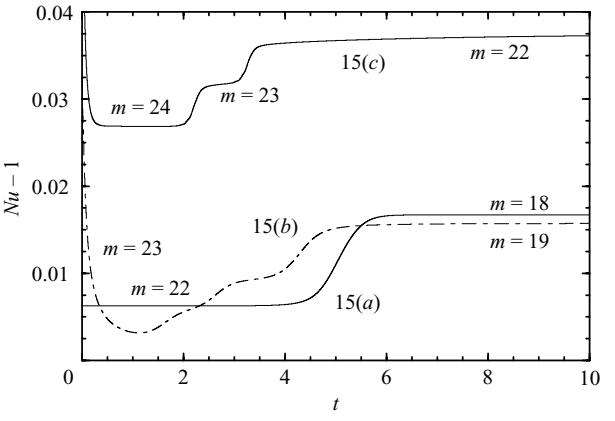

FIGURE 16. Time variation of the Nusselt number for the evolutions shown in figure 15.

mode in the roto-reflection subspace and then determining its stability to general perturbations.

The rotating wave convective states are wall modes, consisting of a periodic array of alternating hot and cold swirling thermal plumes confined to a thin boundary layer at the cylinder sidewall. There is a variety of available stable plume sizes, those with azimuthal wavenumber in the interior of the EBF curve. These states are born in Hopf bifurcations at the marginal stability curve (solid curve with • in figure 3), but only the rotating wave with $m = 18$ is born stable; the other rotating waves stabilize in a sequence of secondary Hopf bifurcations (figure 5). This process is analogous to the sequence of pitchfork bifurcations discussed in Tuckerman & Barkley (1990) in the context of the Ginzburg–Landau equation.

For pure rotating wave states, the azimuthal wavenumber must be an integer as the azimuthal direction is periodic. However, mixed-mode states between wall modes with different azimuthal wavenumbers exist, but are usually unstable. They appear at the secondary Hopf bifurcations associated with the EBF instability. These mixed states govern the transient behaviour observed when stable wall modes cross the EBF curve and become unstable, as we have illustrated in § 3.4. Liu & Ecke (1999) showed that these very slow transients are approximately described by the phase dynamics of the complex Ginzburg–Landau (cGL) equation. They also showed that quintic terms must be added to the cGL equation in order to account for their experimental observations at moderate $\epsilon \approx 0.2$ values. The coefficients of these quintic terms must be adjusted to fit the observations. As the cGL equation is an approximation valid only for small ϵ values, i.e. close to the minimum of the EBF curve, it is likely that additional higher-order terms should be added for larger values of ϵ.

To unravel all the details of the dynamics discussed in § 3.4, direct numerical simulations of the Navier–Stokes equations, like those presented in this paper, are necessary. The computational costs presently limit these computations to moderate aspect ratio containers (our computations have $\gamma = 4$), where they have been useful in exploring the high Coriolis force effects in the absence of centrifugal force effects and at Rayleigh numbers well beyond the onset of convection. For large-aspect-ratio containers ($\gamma > 10$), computations are expensive and the cGL approximation becomes a convenient tool to describe the dynamics. However, in large-aspect-ratio containers, the centrifugal force effects become more important and these can alter the dynamics.

Stimulating discussions with R. E. Ecke are very much appreciated. This work was supported by the National Science Foundation grant DMS-0505489, the Spanish grants FIS2004-01336 and FIS2006-08954, and Catalan grant SGR-00024. Computational resources of ASU's Fulton HPCI are greatly appreciated.

REFERENCES

Ahlers, G., Cannell, D. S., Dominguez-Lerma, M. A. & Heinrichs, R. 1986 Wavenumber selection and Eckhaus instability in Couette–Taylor flow. *Physica* D **23**, 202–219.

Bajaj, K. M. S., Liu, J., Naberhuis, B. & Ahlers, G. 1998 Square patterns in Rayleigh–Bénard convection with rotation about a vertical axis. *Phys. Rev. Lett.* **81**, 806–809.

Benjamin, T. B. & Feir, J. E. 1967 Disintegration of wave trains on deep water. 1. Theory. *J. Fluid Mech.* **27**, 417–430.

Bodenschatz, E., Pesch, W. & Ahlers, G. 2000 Recent developments in Rayleigh–Bénard convection. *Annu. Rev. Fluid Mech.* **32**, 709–778.

Buell, J. C. & Catton, I. 1983 Effect of rotation on the stability of a bounded cylindrical layer of fluid heated from below. *Phys. Fluids* **26**, 892–896.

Chandrasekhar, S. 1961 *Hydrodynamic and Hydromagnetic Stability*. Oxford University Press.

Choi, W., Prasad, D., Camasa, R. & Ecke, R. E. 2004 Traveling waves in rotating Rayleigh–Bénard convection. *Phys. Rev.* E **69**, 056301.

Ecke, R. E., Zhong, F. & Knobloch, E. 1992 Hopf-bifurcation with broken reflection symmetry in rotating Rayleigh–Bénard convection. *Europhys. Lett.* **19**, 177–182.

Eckhaus, W. 1965 *Studies in Nonlinear Stability Theory*. Springer.

Fornberg, B. 1998 *A Practical Guide to Pseudospectral Methods*. Cambridge University Press.

Goldstein, H. F., Knobloch, E., Mercader, I. & Net, M. 1993 Convection in a rotating cylinder. Part 1. Linear theory for moderate Prandtl numbers. *J. Fluid Mech.* **248**, 583–604.

Goldstein, H. F., Knobloch, E., Mercader, I. & Net, M. 1994 Convection in a rotating cylinder. Part 2. Linear theory for low Prandtl numbers. *J. Fluid Mech.* **262**, 293–324.

Herrmann, J. & Busse, F. H. 1993 Asymptotic theory of wall-attached convection in a rotating fluid layer. *J. Fluid Mech.* **255**, 183–194.

Hu, Y., Ecke, R. E. & Ahlers, G. 1997 Convection under rotation for Prandtl numbers near 1. Linear stability, wave-number selection, and pattern dynamics. *Phys. Rev.* E **55**, 6928–6949.

Hughes, S. & Randriamampianina, A. 1998 An improved projection scheme applied to pseudospectral methods for the incompressible Navier–Stokes equations. *Intl J. Numer. Meth. Fluids* **28**, 501–521.

Janiaud, B., Pumir, A., Benisom, D., Croquette, V., Richter, H. & Kramer, L. 1992 The Eckhaus instability for traveling waves. *Physica* D **55**, 269–286.

Knobloch, E. 1994 Bifurcations in rotating systems. In *Lectures on Solar and Planetary Dynamos* (ed. M. R. E. Proctor & A. D. Gilbert), pp. 331–372. Cambridge University Press.

Krupa, M. 1990 Bifurcations of relative equilibria. *SIAM J. Math. Anal.* **21**, 1453–1486.

Kuo, E. Y. & Cross, M. C. 1993 Traveling-wave wall states in rotating Rayleigh–Bénard convection. *Phys. Rev.* E **47**, R2245–R2248.

Kuznetsov, Y. A. 1998 *Elements of Applied Bifurcation Theory*, 2nd edn. Springer.

Liu, Y. & Ecke, R. E. 1997 Eckhaus–Benjamin–Feir instability in rotating convection. *Phys. Rev. Lett.* **78**, 4391–4394.

Liu, Y. & Ecke, R. E. 1999 Nonlinear traveling waves in rotating Rayleigh–Bénard convection: stability boundaries and phase diffusion. *Phys. Rev.* E **59**, 4091–4105.

Lopez, J. M., Hart, J. E., Marques, F., Kittelman, S. & Shen, J. 2002 Instability and mode interactions in a differentially-driven rotating cylinder. *J. Fluid Mech.* **462**, 383–409.

Marques, F. & Lopez, J. M. 2001 Precessing vortex breakdown mode in an enclosed cylinder flow. *Phys. Fluids* **13**, 1679–1682.

Marques, F., Lopez, J. M. & Shen, J. 2002 Mode interactions in an enclosed swirling flow: a double Hopf bifurcation between azimuthal wavenumbers 0 and 2. *J. Fluid Mech.* **455**, 263–281.

Mercader, I., Net, M. & Falqués, A. 1991 Spectral methods for high order equations. *Comput. Meth. Appl. Mech. Engng* **91**, 1245–1251.

Mizushima, J. & Fujimura, K. 1992 Higher harmonic resonance of two-dimensional disturbances in Rayleigh–Bénard convection. *J. Fluid Mech.* **234**, 651–667.

Nagata, M. 1995 Bifurcations at the Eckhaus points in two-dimensional Rayleigh–Bénard convection. *Phys. Rev.* E **52**, 6141–6145.

Ning, L. & Ecke, R. E. 1993 Rotating Rayleigh–Bénard convection: aspect-ratio dependence of the initial bifurcations. *Phys. Rev.* E **47**, 3326–3333.

Orszag, S. A. & Patera, A. T. 1983 Secondary instability of wall-bounded shear flows. *J. Fluid Mech.* **128**, 347–385.

Pfotenhauer, J. M., Niemela, J. J. & Donnelly, R. J. 1987 Stability and heat transfer of rotating cryogens. Part 3. Effects of finite cylindrical geometry and rotation on the onset of convection. *J. Fluid Mech.* **175**, 85–96.

Plaut, E. 2003 Nonlinear dynamics of traveling waves in rotating Rayleigh–Bénard convection: effects of the boundary conditions and of the topology. *Phys. Rev.* E **67**, 046303.

Porter, J. & Knobloch, E. 2000 Complex dynamics in the 1:3 spatial resonance. *Physica* D **143** (1–4), 138–168.

Prat, J., Mercader, I. & Knobloch, E. 1998 Resonant mode interactions in Rayleigh–Bénard convection. *Phys. Rev.* E **58**, 3145–3156.

Rand, D. 1982 Dynamics and symmetry. Predictions for modulated waves in rotating fluids. *Arch. Rat. Mech. Anal.* **79**, 1–38.

Rossby, H. T. 1967 A study of Bénard convection with and without rotation. *J. Fluid Mech.* **29**, 673–690.

Rüdiger, S. & Feudel, F. 2000 Pattern formation in Rayleigh–Bénard convection in a cylindrical container. *Phys. Rev.* E **62**, 4927–4931.

Rüdiger, S. & Knobloch, E. 2003 Mode interaction in rotating Rayleigh–Bénard convection. *Fluid Dyn. Res.* **33**, 477–492.

Sánchez-Álvarez, J. J., Serre, E., Crespo del Arco, E. & Busse, F. H. 2005 Square patterns in rotating Rayleigh–Bénard convection. *Phys. Rev.* E **72**, 036307.

Scheel, J. D., Paul, M. R., Cross, M. C. & Fischer, P. F. 2003 Traveling waves in rotating Rayleigh–Bénard convection: analysis of modes and mean flow. *Phys. Rev.* E **68**, 066216.

Tuckerman, L. S. & Barkley, D. 1990 Bifurcation analysis of the Eckhaus instability. *Physica* D **46**, 57–86.

Zhong, F., Ecke, R. & Steinberg, V. 1991 Asymmetric modes and the transition to vortex structures in rotating Rayleigh–Bénard convection. *Phys. Rev. Lett.* **67**, 2473–2476.

Zhong, F., Ecke, R. & Steinberg, V. 1993 Rotating Rayleigh–Bénard convection: asymmetric modes and vortex states. *J. Fluid Mech.* **249**, 135–159.